AN EXPERIMENTAL DATABASE FOR THE ANALYSIS OF BURSTING OF A LAMINAR SEPARATION BUBBLE

M. Dellacasagrande, D. Lengani, D. Simoni, M. Ubaldi

DIME, University of Genova, Genova 16145, Italy

ABSTRACT

The bursting phenomenon consists in the switch of a laminar separation bubble from a short to a long configuration. In the former case, reduced effects on the profile pressure distribution are typically observed with respect to the attached condition. On the contrary, long bubbles provoke significant variations of the loading coefficient upstream of the separation position, with increased risk of stall. The present work presents an experimental database on separated-flow transitional boundary layers under different Reynolds numbers, adverse pressure gradients and turbulence intensity levels (Tu=1.5%, 2.5%, 3.5%). Overall, more than 90 flow conditions were tested concerning short and long bubbles for the characterization of separated flows under turbine-like conditions. Measurements were performed on a flat plate geometry using a fast response particle image velocimetry (PIV) system. For each flow case, two sets of 6000 snapshots were acquired at a sampling rate of 300 and 1000 Hz. Based on existing criteria for the identification of the bursting phenomenon, the flow cases were clustered in terms of short and long bubble states. Additionally, the kind of instability (i.e. convective or absolute) developing into the separated boundary layer was identified based on time-mean flow quantities. The present study highlights the existing link between the bursting of a laminar separation bubble and the onset of the absolute instability of the separated shear layer, with stationary vortices forming in the dead air region.

KEYWORDS

Boundary layer flows, PIV, Laminar separation bubble, Bubble bursting

NOMENCLATURE

Re_L	Reynolds number based on plate length
Tu	Free-stream turbulence intensity
APG	Adverse Pressure Gradient
AP	Acceleration parameter
L	Plate length
LSB	Laminar Separation Bubble
R_{uu}	Streamwise auto-correlation function
h_r	Recirculating region height
δ^*	Boundary layer displacement thickness
θ	Boundary layer momentum thickness
α	Opening angle of the top-wall of the channel
ν	Kinematic viscosity

INTRODUCTION

Under strong adverse pressure gradients (APG), low turbulence intensity (Tu) levels and low Reynolds numbers, boundary layer (BL) separation may occur with the consequent increment of losses. If the boundary layer reattaches before the end of the profile, a laminar separation bubble (LSB) is formed. Applications that operate under this particular flow configuration include unmanned aerial vehicles, low-pressure turbines, low-pressure compressors, helicopter blades, and wind turbines. In this context, it is of great interest to know the flow conditions under which a relatively $short$ bubble switches into a $long$ one, with the massive modification of the profile pressure distribution and the increased risk of stall. This sudden modification of the bubble state is termed in the literature as the bubble $bursting$ (Marxen and Henningson 2011). Because bubble bursting is a deleterious phenomenon, a large amount of efforts have been made over the past decades for its understanding and, especially, for the construction of empirical criteria aimed at its prediction (see e.g. Von Doenhoff 1938; Owen and Klanfer 1953; Crabtree 1959). A detailed analysis of the bursting process has been carried out in the pioneering work of Gaster (1967), where a two parameters criterion has been proposed for the prediction of the modification of the bubble state. The author performed several experiments on a flat plate with variable Reynolds number and pressure gradient, thus finally highlighting the existing correlation between the momentum thickness Reynolds number at separation and the non-dimensional parameter $P_G = \theta_s^2/\nu(\Delta U/\Delta X)$. The P_G parameter introduced by Gaster (1967) takes into account for the momentum thickness at separation (θ_s) and the velocity gradient across the bubble length with reference to an attached flow condition. In the more recent works of Diwan et al (2006) and Mitra and Ramesh (2019) a single-parameter criterion has been proposed based on the newly defined quantity $P_{DCR} = h^2/\nu(\Delta U/\Delta X)_{act}$. Diwan et al (2006) therefore introduced the maximum bubble height (h) as influencing parameter for the identification of the bubble state. Additionally, $(\Delta U/\Delta X)_{act}$ is the actual velocity gradient between the separation and the reattachment locations. When $P_{DCR} < -28$, bursting is expected to occur. The criterion proposed by Diwan et al (2006) has been adopted in successive literature works concerning external aerodynamic at very low turbulence levels (see e.g., Serna and Lázaro 2015; Alferez et al 2013). In this context, Alferez et al (2013) inferred that the bursting process may be initiated by the modification of the shear layer characteristics due to the increased distance from the wall, rather than by the change in the nature of the instability from convective to absolute, contrarily to what was originally supposed by Gaster (1967). Among others, Almutairi et al (2010) performed numerical simulations of LSB undergoing bursting at a very low Reynolds number. The authors found the bubble bursting to be more irregular compared to previous experimental works at higher Reynolds numbers. In the more recent work of Eljack et al (2021) low-frequency oscillations of a LSB forming over an airfoil has been found to precede the complete profile stall. Then, the above mentioned works clearly highlight the complexity of the bursting phenomenon, which is still far to be completely understood. Indeed, the role of the different flow parameters on the bursting process is mostly obtained by comparison of different literature works, concerning both experiments and numerical simulations.

The present paper describes a newly acquired experimental data base on laminar separation bubbles forming on a flat plate for different Tu levels and pressure gradients. For each combination of these two parameters, about ten different Reynolds numbers have been tested, which allowed the observation of both short and long bubble states. Overall, about 90 flow conditions have been acquired by means of Particle Image Velocimetry. Measurements have been performed at elevated sampling rate and spatial resolution, thus allowing to solve with great details

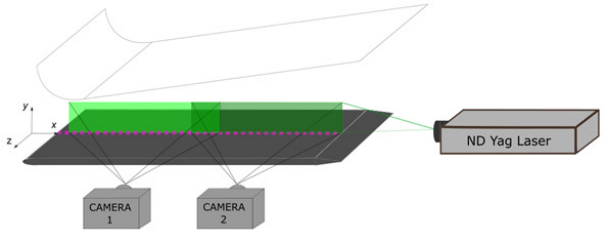

Figure 1: Test section and PIV instrumentation layout.

the spatio-temporal fluctuations whose growth leads to the turbulent state of the boundary layer and its consequent reattachment. Due to the detailed measurements here performed, the present data set is therefore aimed at the characterization of the statistical evolution of the separation induced transition, for both short and long bubble states, as well as at the inspection of the dominant flow dynamics and their related stability characteristics. Data presented in this work are available upon request to the authors.

EXPERIMENTAL SETUP AND MEASURING TECHNIQUES

The present data base has been collected in the wind tunnel of the Aerodynamic and Turbomachinery laboratory of the University of Genova. The wind tunnel has been operated at low speed with Mach number far below 0.1. Nevertheless, the acquired data are representative also of LSBs evolving at high-speed provided that shock-induced separation does not occur and the same effective APGs are considered. Shock induced boundary layer separation is indeed substantially different from that induced by a continuous APG distribution. For the present experiments, a flat plate with a $4:1$ elliptic leading edge has been installed between two adjustable endwalls, whose opening angle can be changed to vary the streamwise pressure gradient imposed to the boundary layer (see figure 1). The flow is accelerated from the plate leading edge up to the channel throat using a converging fixed geometry. Then, the pressure gradient can be modified in the rear part of the plate. The opening angle of the top endwall (α) has been set to 7, 9 and 12 degrees, which correspond to the values of -0.18, -0.27 and -0.41 of the acceleration parameter $AP = \frac{L}{U_{\infty,0}} \frac{\Delta U_\infty}{\Delta x}$. This latter is defined based on the plate length L, the free-stream velocity at the channel throat ($U_{\infty,0}$) and the overall velocity gradient along the rear part of the plate. The plate length and width are equal to 300mm to obtain 2D time-mean flow at the mid-section of the channel, where PIV measurements have been carried out.

The free-stream turbulence intensity has been controlled using turbulence generating grids located 500mm upstream of the plate leading edge. The root mean square of velocity fluctuations has been measured by means of Laser Doppler Velocimetry (LDV) at the inlet section of the test section. Velocity data has been acquired in the free-stream region at a mean sampling rate of 10kHz over a sampling period equal to 120s. Table 1 reports the geometric parameters of the grids adopted, the corresponding Tu level and the streamwise integral length-scale (L_x). This latter has been computed by means of the auto-correlation function of LDV data collected at the plate leading edge under the Taylor's hypothesis of frozen turbulence. The lowest Tu level is provided by the spontaneous turbulence of the tunnel. For each combination of the free-stream turbulence and the pressure gradient, about 10 Reynolds numbers (Re_L) have been tested. This latter parameter is defined based on the plate length and the free-stream velocity

Table 1: Turbulence-generating grids characterization: free-stream turbulence intensity (Tu), bars width (d), mesh size (M), porosity parameter $P = (1 - d/M)^2$ and streamwise integral length scale L_x.

$Case$	Tu [%]	d [mm]	M [mm]	P	L_x [mm]
No-Grid	1.5%	-	-	-	6.2
Low-Tu	2.5%	2	8	0.64	11.5
High-Tu	3.5%	4	8	0.36	13.2

at the plate leading edge. The so defined Reynolds number is adopted hereafter for the identification of the different flow conditions. Other BL-based Reynolds numbers can be computed from the current dataset such as the momentum or displacement thickness Reynolds numbers. These latter can be used as main ingredients for the construction of empirical correlations for transition as well as for comparison with numerical simulations of the present flow cases. The overall test matrix consists of almost 90 flow conditions concerning the systematic variation of the main influencing parameters.

PIV measurements have been performed in this work in a wall-normal plane aligned with the meridional section of the plate. To reduce laser reflections, the plate has been black painted and the laser incidence angle has been minimized by positioning the laser optics far behind the plate trailing edge, instead of illuminating the plate from the top side of the test section. Two cameras have been used simultaneously to acquire the evolution of the boundary layer from the channel throat to the end of the plate. This guaranteed that the entire evolution of the laminar separation bubbles forming over the plate surface has been recorded for the overall combinations of the above mentioned parameters. Moreover, using two camera allowed us to extend the field of view while keeping the spatial resolution sufficiently high to solve with great details the dominant coherent structures within the flow. The PIV system adopted is a dual-cavity ND:YLF pulsed laser Litron LDY 300 (energy 30 mJ per pulse at 1000 Hz repetition rate, 527 nm wavelength). Two high sensitive SpeedSense M340 digital cameras with a cooled 2560 x 1600 pixels CMOS matrix have been used for the acquisition of the overall velocity field. For the present experiments, the magnification factor was set to about 0.16. A multi-grid algorithm has been adopted for the computation of the adaptive cross-correlation of PIV images: a first interrogation area of 32x32 pixels is used with a successive refinement to 16x16 pixels and 50% overlap. This corresponds to a vector grid spacing of 0.41 mm. A peak validation has been used to discriminate between valid and invalid vectors. A Gaussian fitting procedure has been also adopted to obtain a sub-pixel recognition accuracy of particle displacement equal to 0.1 pixel. Based on the works of Sciacchitano et al (2015) and Wieneke (2015), the uncertainty in the instantaneous velocity measurement is expected to be smaller than 3% in the free-stream region and it grows to 6% in the boundary layer. Among the methods compared in the paper of Sciacchitano et al (2015), the uncertainty estimation of the measured velocity field has been carried out considering the peak-ratio method proposed by Charonko and Vlachos (2013). This method is implemented in the commercial software DynamicStudio 7.3 adopted for the current measurements (see also Canepa et al 2018, 2019). The method correlates the particle displacement uncertainty to the ratio between the dominant correlation peak and the second highest one, thus providing instantaneous maps of the uncertainty for the measured particle displacement,

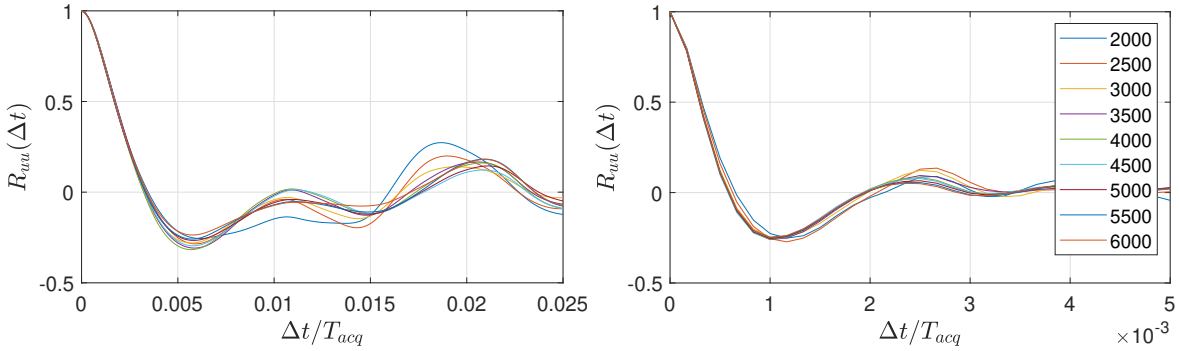

Figure 2: Temporal auto-correlation function of velocity fluctuations for the cases (left) $Re_L = 21017 - Tu = 1.5\% - \alpha = 12$ and (right) $Re_L = 66173 - Tu = 1.5\% - \alpha = 12$. The auto-correlation functions have been obtained from the data-set sampled at 1 kHz over an acquisition period of 6 seconds. The time shift is scaled with the overall acquisition period. Different curves refer to the different number of snapshots adopted for the computation of the auto-correlation function.

from which the velocity uncertainty values have been computed. Additionally, complementary analysis of the effects due to near wall velocity gradient has been performed following the work of Wilson and Smith (2013).

For each combination of the flow parameters, two sets of 6000 snapshots have been acquired at a sampling rate of 1000 and 300 Hz. In order to verify the statistical reliability of the data, a convergence analysis has been carried out based on the temporal auto-correlation function of the fluctuating velocity components. Figure 2 shows exemplary auto-correlation functions for a low (left) and a high (right) Reynolds numbers at the maximum pressure gradient and the lowest Tu level, i.e. α=12 and Tu=1.5%. This represents the most burdensome combination of APG and Tu level for the occurrence of the bubble bursting. The colored curves reported in figure 2 refer to different numbers of PIV snapshots adopted for the computation of the auto-correlation function. Data reported in figure 2 clearly indicate that the characteristic period of the main coherent fluctuations is well captured using only 3000 snapshots (see the position of the first negative peak in the auto-correlation function). It should be noted that the time shift (Δt) is normalized by the overall acquisition period (T_{acq}). Accordingly, about 100 to 500 bubble cycles have been acquired from the lowest to the highest Reynolds numbers at a sampling rate of 1 kHz. For the highest Reynolds numbers, the bubble time-scale has been discretized with about 20 sample points, which increase to about 70 for the lowest Re_L values. Further details on the adopted test section and measuring techniques can be found in the previous works Verdoya et al (2021) and Canepa et al (2021).

TIME-MEAN FLOW FIELDS AND BOUNDARY LAYER STATISTICAL PARAMETERS

In order to highlight the response of the laminar separation bubble to the flow parameter variation, this section reports some statistical quantities of the separated boundary layer for selected flow cases among those tested.

Figure 3 shows the contour plots of the normalized streamwise velocity component (u/U_e) at fixed Tu=1.5% and α=12 for variable Reynolds numbers. This latter is indeed the parameter

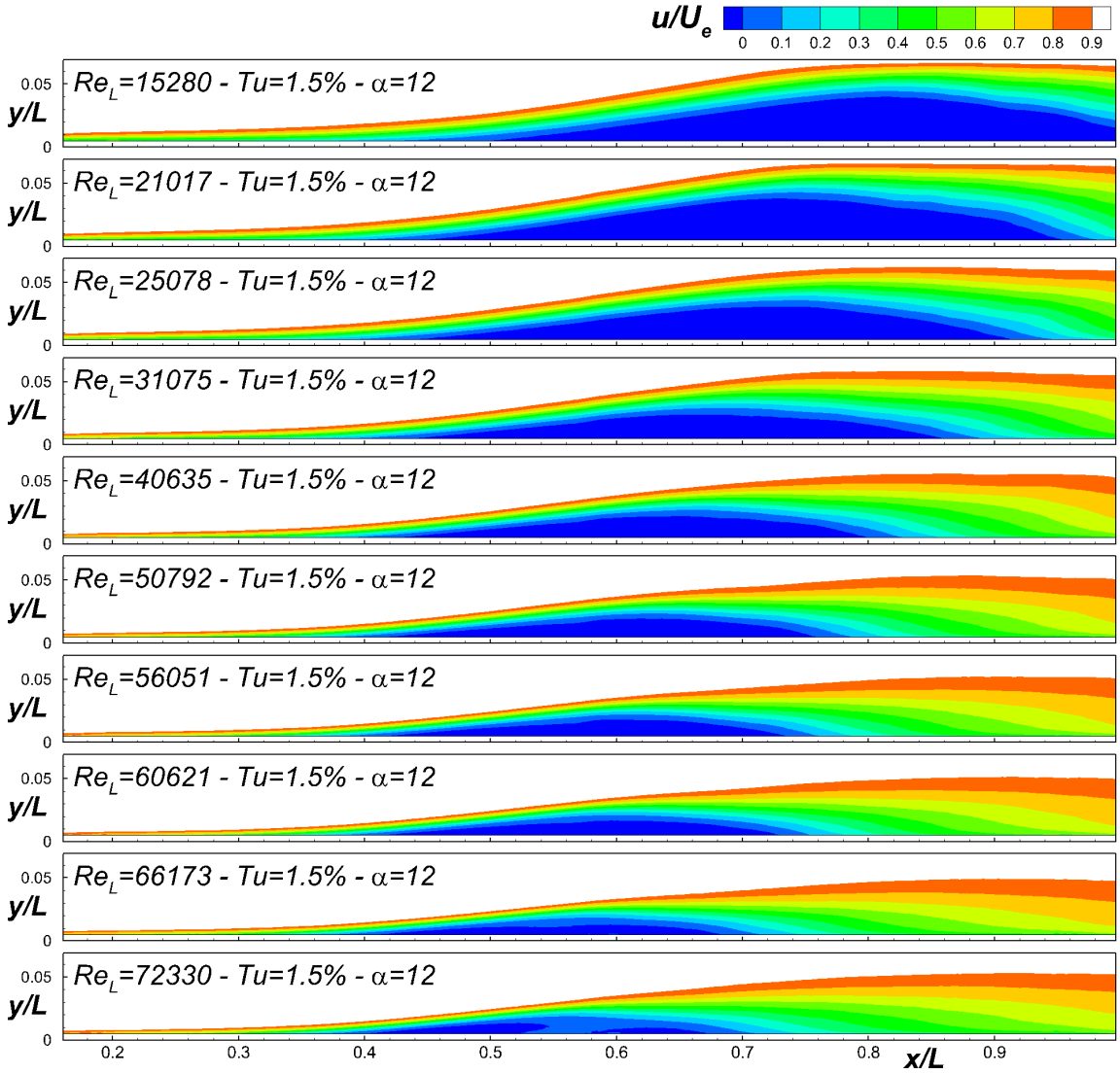

Figure 3: Normalized time-mean velocity (u/U_e) for variable Reynolds number at fixed $Tu = 1.5\%$ and $\alpha = 12°$.

showing the greatest influence on the definition of the bubble state (i.e. *short* and *long* one). Similar time-mean velocity distributions have been indeed obtained for the other combinations of the pressure gradient and Tu level, not shown here for brevity. Results reported in figure 3 clearly highlight the increase in the bubble size with the reduction of the Reynolds number. Particularly, moving from the bottom to the top plot the acquired flow field switches from a very short bubble to an open one, for which the turbulent reattachment does not occur before the end of the plate. The boundary layer separation occurs for all cases in the range $0.39 < x/L < 0.42$, thus the growth of the bubble length is due to the downstream shift of the bubble maximum displacement and reattachment positions. Interestingly, for $Re_L < 40635$, the growth rate of the bubble due to the Reynolds number reduction significantly increases (the Reynolds number was almost uniformly sampled). This sudden increment of the bubble size can be directly ascribed to the occurrence of the bursting process, as further discussed in the following, thus a critical Reynolds number has been identified for the different flow cases.

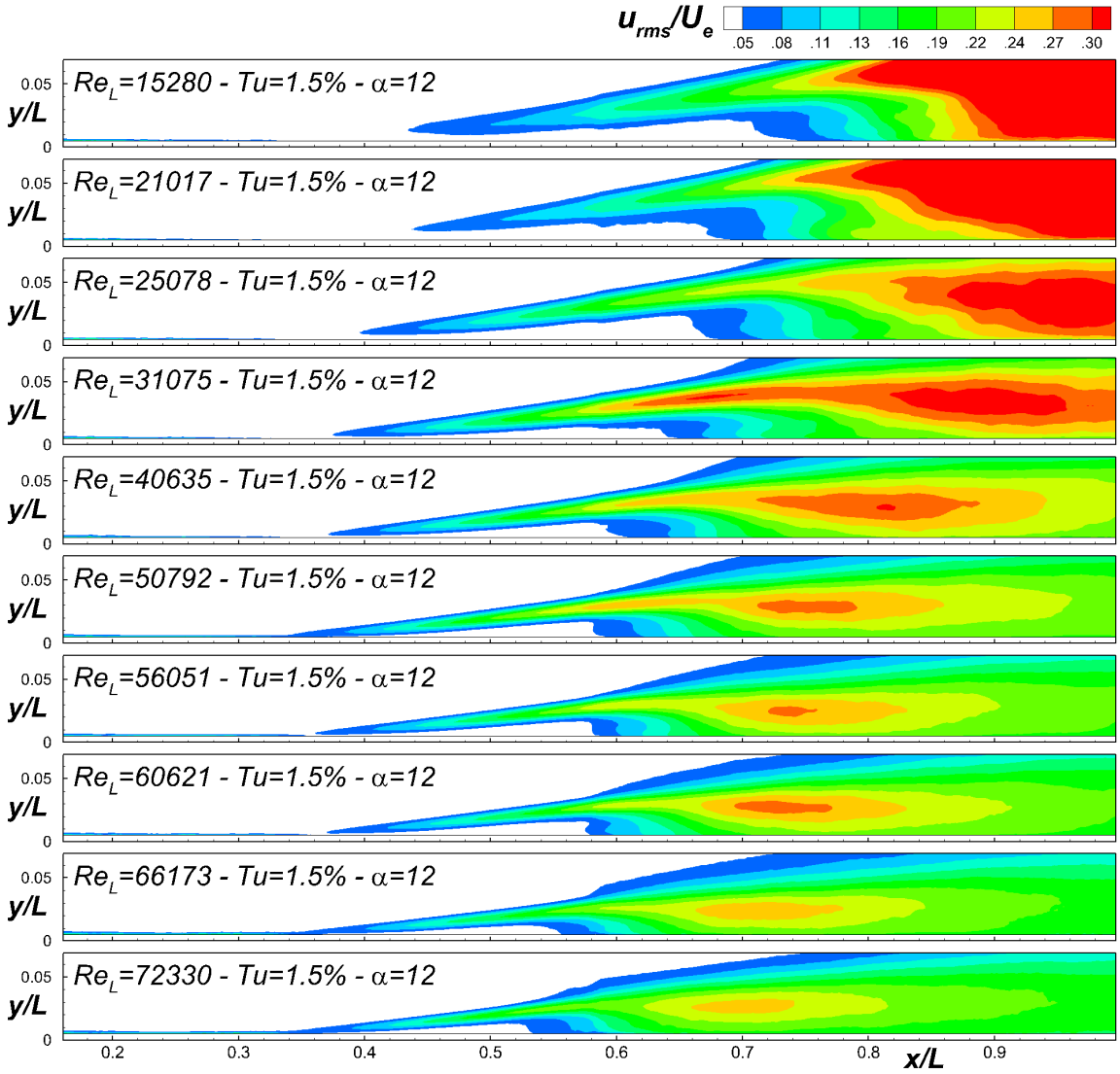

Figure 4: Normalized root mean square of velocity fluctuations (u_{rms}/U_e) for variable Reynolds number at fixed $Tu = 1.5\%$ and $\alpha = 12°$.

Figure 4 shows the contour plots of the root mean square (rms) of the streamwise velocity fluctuations (u_{rms}/U_e) for the same cases reported in figure 3. The region where the maximum rms values occur is seen to move downstream as the Reynolds number is reduced, according to the increment of the bubble length. Additionally, the saturation level of the rms of fluctuations becomes increasingly higher as Re_L is reduced. This is due to the occurrence of significantly larger vortices which are responsible for higher levels of fluctuations. As it will be shown in the following section, the range of Reynolds number variation here tested has been found to cause a substantial modification of the leading structures observed near the bubble maximum displacement, where the maximum rms values occur. Moreover, the growth of fluctuations in the fore part of the bubble will be shown to reduce at low Re_L values, which is the cause for the delayed transition and reattachment.

In order to synthesise the effects due to the flow parameter variation on the time-mean shape of the laminar separation bubble and its stability characteristics, figure 5 reports the streamwise

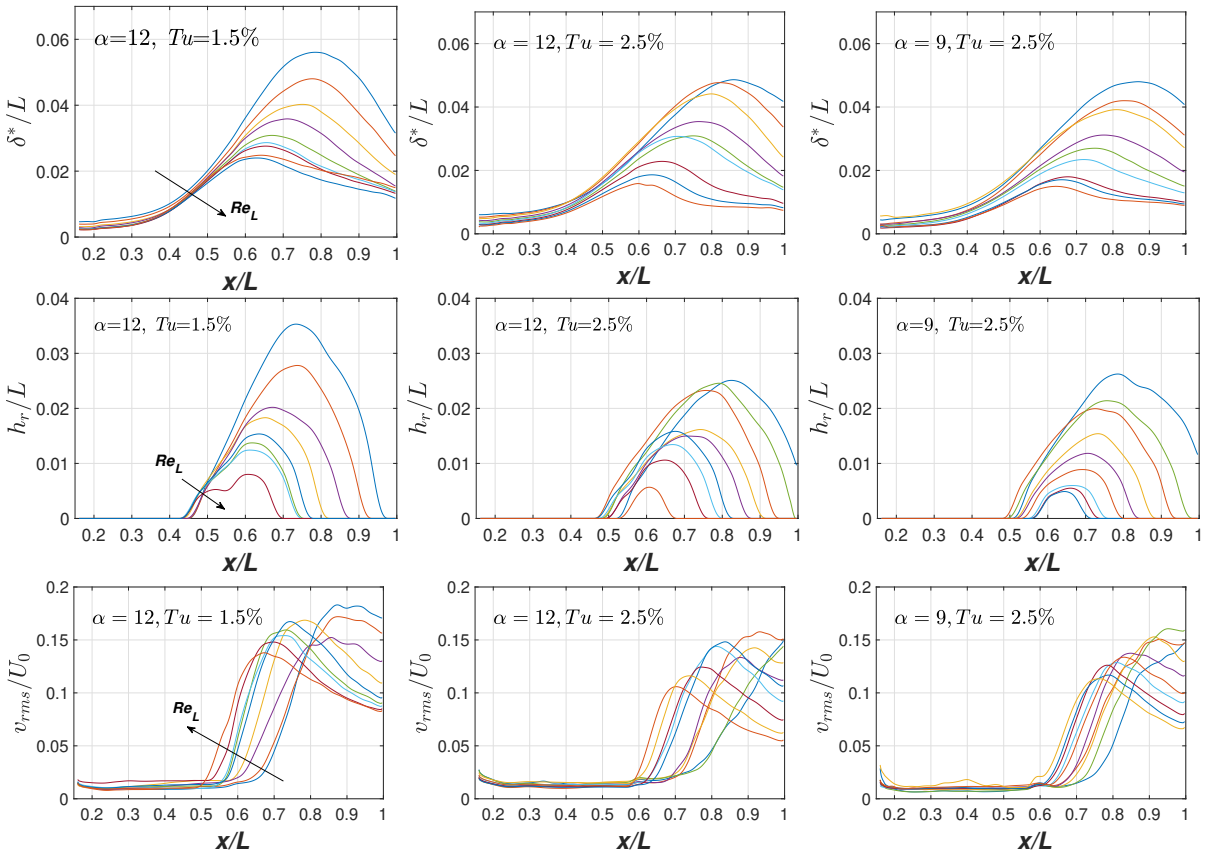

Figure 5: Streamwise variation of the displacement thickness scaled with the plate length (top, δ^*/L), of the recirculating height scaled with the plate length (center, h_r/L) and of the rms of normal to the wall fluctuations scaled with the inlet free-stream velocity (bottom, v_{rms}/U_0). From left to right: $\alpha = 12 - Tu = 1.5\%$, $\alpha = 12 - Tu = 2.5\%$ and $\alpha = 9 - Tu = 2.5\%$. The Reynolds variation effect is highlighted in each plot.

distributions of the non-dimensional BL displacement thickness (δ^*/L, top plots) and of the recirculating height (h_r/L, center plots) for the cases $\alpha = 12 - Tu = 1.5\%$, $\alpha = 12 - Tu = 2.5\%$ and $\alpha = 9 - Tu = 2.5\%$ (from left to right). Additionally, the distributions of the local maxima of the rms of normal to the wall fluctuations (v_{rms}/U_0) are reported in the bottom plots of the same figure. The growth of this quantity is directly linked to the onset of transition (see e.g., Dellacasagrande et al 2020b), thus the v_{rms}/U_0 distributions highlight the role of the flow parameters on the amplification of disturbances leading to the turbulent state of the boundary layer. The effect of the Reynolds number variation is presented in each plot within the same range of Re_L values.

The displacement thickness distributions (top plots) show substantially the same trend in the first part of the measuring domain when varying the Reynolds number at fixed APG and Tu level. Higher values of δ^*/L are observed near the domain inlet at lower Re_L due to the thickening of the BL, as expected. When comparing the cases $\alpha = 12 - Tu = 1.5\%$ and $\alpha = 12 - Tu = 2.5\%$ (i.e. increasing the free-stream turbulence), one can see that the increment of the Tu level leads to a reduced growth of δ^*/L upstream of the separation position, i.e. before the curves significantly diverge from each other. Moreover, a similar effect is observed reducing the streamwise pressure gradient (compare the cases $\alpha = 12 - Tu = 2.5\%$ and

$\alpha = 9 - Tu = 2.5\%$). On one hand, the disturbances forming in the laminar boundary layer under elevated free-stream turbulence act increasing the capability of the BL to overcome the adverse pressure gradient. Otherwise, the reduction of the opening angle of the channel leads to lower velocity gradient and reduced boundary layer growth. This leads to a delayed detachment position according to the separation criteria presented in the literature (e.g., Curle and Skan 1957). Moving towards the end of the plate, the curves significantly diverge from each other for the different combinations of Tu levels and APG, thus showing the effects due to the Reynolds number variation on the maximum bubble height and its location. The maximum peak of δ^*/L moves upstream and significantly reduces as the flow Reynolds number is increased, as widely discussed in previous literature works (e.g., Istvan et al 2018, Dellacasagrande et al 2020a).

The distributions of h_r/L reported in the center plots of figure 5 further highlight the effects due to the flow parameter variation on the separation and reattachment positions. At the lowest Tu level (left plot), the separation position is shown to be substantially the same for the different Re_L values, accordingly to the contour plots depicted in figure 3. A delayed separation is observed instead when increasing the Tu level (from the left to the center plot), as well as reducing the APG (from the center to the right plot), and the role of Re_L variation becomes more relevant. However, the dominant effect still concerns the modification of the reattachment position and the bubble height. It should be noted that below a certain Re_L value, a sudden growth of the bubble dimension occurs, which has been found to be representative of the occurrence of bursting. A similar behavior has been indeed observed for the other combinations of the flow parameters here tested, which further indicates the presence of different bubble states within the current data set.

Finally, the distributions of v_{rms}/U_0 (bottom plots) can be used to highlight the possibility of inspecting the dynamic properties of the laminar separation bubbles. For all APG and Tu levels, the point at which the amplification of the rms of fluctuations occurs moves upstream as the Reynolds number increases, which highlights the anticipation of the laminar to turbulent transition. This is also confirmed by the upstream shift of the streamwise position at which v_{rms}/U_0 saturates for the different cases, which occurs near the bubble maximum displacement position. Moreover, the higher the Re_L the higher the spatial growth of v_{rms}/U_0, which denotes a modification of the stability characteristics of the separated shear layer (see e.g., Simoni et al 2017). Again, a Re_L value there exists below which a marked modification, i.e. reduction, of the v_{rms}/U_0 growth is observed. Data reported in figure 5 make clear that this behavior is linked to the increment of the bubble size (see the h_r/L distributions). The growth rate of fluctuations is found to reduce also at lower APG, while the Tu level has minor effects in this sense.

INSTANTANEOUS PERTURBATION VELOCITY FIELDS

The present section presents exemplary PIV snapshots to highlight the possibility of further characterizing the main structures driving the transition process of a laminar separation bubble. Since the bubble state has been found to be mostly affected by the flow Reynolds number, figure 6 shows instantaneous vector maps of the fluctuating velocity field for the cases $Re_L = 66173 - Tu = 1.5\% - \alpha = 12$ (top) and $Re_L = 21017 - Tu = 1.5\% - \alpha = 12$ (bottom), thus showing the effects of Re_L on the main coherent structures developing within the bubble. The high Re_L case reported in figure 6 shows the occurrence of counter rotating vortices forming near the bubble maximum displacement (blue circles in the plots). These structures are seen to grow as they move in the main flow direction, being convectively amplified. Then, the presence of smaller structures for $x/L > 0.75$ indicates the occurrence of vortex breakup and

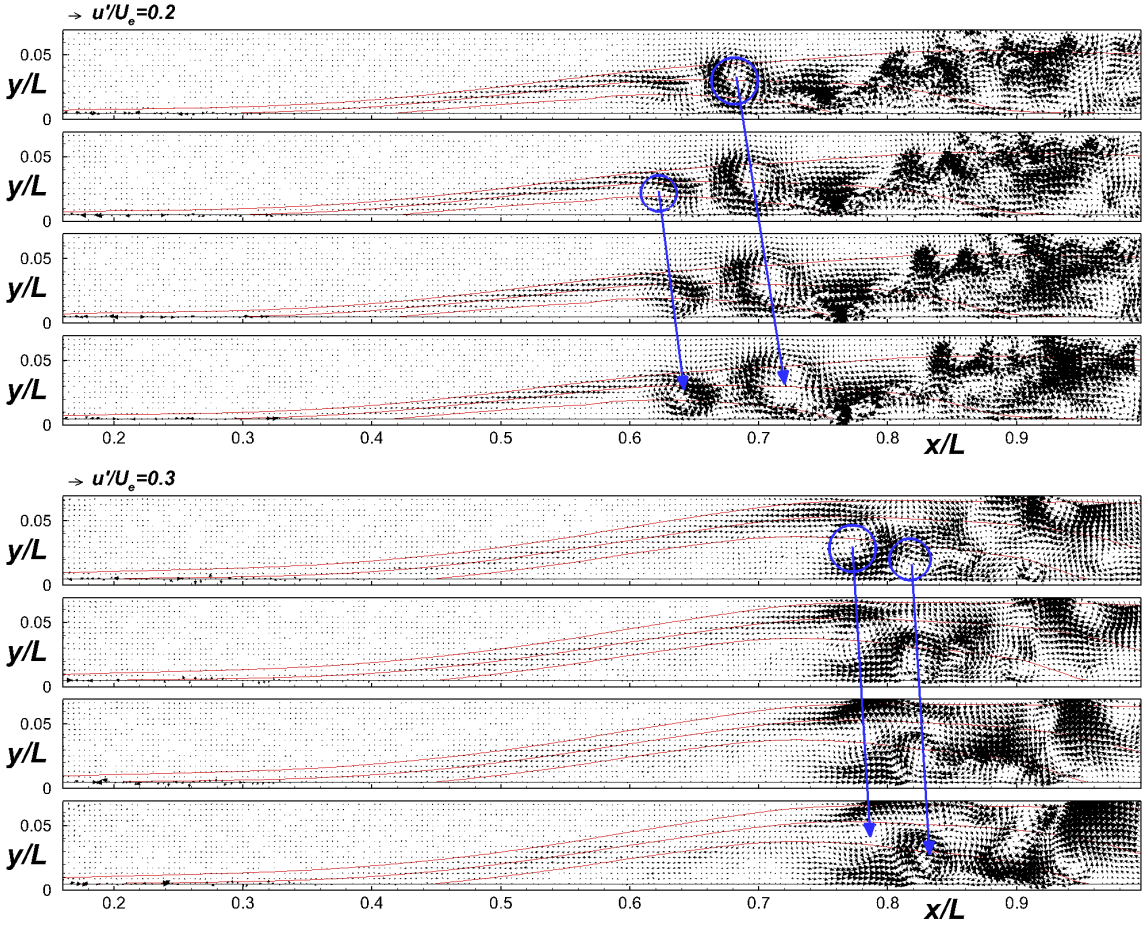

Figure 6: Instantaneous vector maps of fluctuating velocity field for the cases (top) $Re_L = 66173 - Tu = 1.5\% - \alpha = 12$ and (bottom) $Re_L = 21017 - Tu = 1.5\% - \alpha = 12$. Iso-contour lines of $u/U_e = 0$, 0.3 and 0.9 are depicted with red color. Blue arrows are adopted to track vortices at the different time instants. One every two measured points is depicted.

transition. What is shown in the top plot of figure 6 is the typical pattern characterising the well-known Kelvin-Helmholtz (K-H) instability process, which drives the convective growth of disturbances in the separated boundary layer.

A different scenario is observed for the low Re_L case presented in the bottom plot of figure 6. Indeed, as the Reynolds number reduces below a certain threshold, the train of counter rotating vortices characterizing the K-H instability no longer occurs, while significantly larger vortices start to form inside the recirculating flow region (see the blue circles in the first plot). These significantly larger scale vortices lead to the increased level of fluctuations highlighted by the rms distributions reported in figure 4. Moreover, vortical structures forming at very low Reynolds numbers have been found to grow in time at almost fixed position (see the blue arrows), instead of being convectively amplified. This indicates a substantial modification of the stability characteristics of the laminar separation bubble, as it has been also highlighted by means of the v_{rms}/U_0 distributions reported in figure 5. Particularly, the absolute instability of disturbances is expected to take place for the low Re_L cases, as further discussed in the following section, with the consequent modification of the growth rate of fluctuations and the

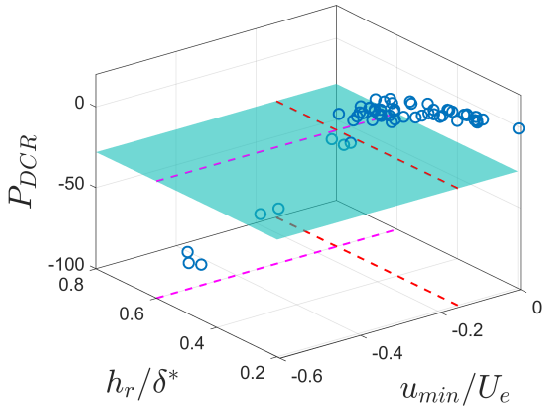

Figure 7: 3D plot of the overall flow cases in terms of the maximum reversed flow velocity (u_{min}/U_e), the non-dimensional height of the recirculating region (h_r/δ^*) and the bursting parameter P_{DCR}.

occurrence of delayed transition and reattachment.

To overcome the limitation of the visual inspection of PIV data, the wavelength and frequency of the main coherent structures shed by the bubble have been computed for each case. A non-dimensional wave-number kl has been defined based on the vortex wavelength (λ) and the shear layer thickness at the separation position (l), i.e. $kl = 2\pi l/\lambda$. This non-dimensional parameter has been found to be equal to about 0.8 in the short bubble regime regardless of Re_L, Tu level and APG. This indicates a self-similarity of the main vortical structures shed by the bubble. Instead, kl significantly deviates from this value when the Reynolds number reduces below a certain threshold. For the cases reported in figure 6, the scaling parameter kl has been found to reduce from 0.82 to 0.44 when passing from the high to the low Re_L condition. Similarly, the group velocity of the dominant coherent vortical structures has been computed and scaled with the local external velocity. The non-dimensional travelling speed of the vortical structures formed in the LSB reduces from about 0.5 in the short regime to null and even negative values in the long one. This is linked to the dominance of temporal growth of fluctuations and the development of vorticity cores in the recirculating region. Again, this indicates a substantial modification of the instability processes driving turbulence generation in the separated shear layer.

DATA CLUSTERING BASED ON THE BUBBLE STATES AND THE BL INSTABILITY CHARACTERISTICS

In this section, statistical parameters defined in previous literature works are used to cluster the current data in terms of short and long bubble types, as well as with reference to the instability mechanisms driving the disturbance growth in the boundary layer. This allows discussing the eventual link between the occurrence of the bubble bursting and the switch of the stability characteristics of the separated shear layer. The bubble state is identified based on the P_{DCR} parameter previously defined by Mitra and Ramesh (2019). Then, two additional parameters have been used for the characterization of the instability process for the different cases examined. The first one is the ratio between the maximum height of the recirculating flow region and the local boundary layer displacement thickness, i.e. h_r/δ^*. According to the work of Maucher et al (2000), when this quantity is higher than 0.6, the absolute instability of fluctuations is expected

to occur. Similarly, the switch from the convective to the absolute instability is expected to take place when the maximum reversed flow is larger than 15% of the local external velocity, that is $u_{min}/U_e < -0.15$ (see Pauley et al 1990; Maucher et al 2000). These two different criteria for the occurrence of the absolute instability of fluctuations are combined in figure 7 with the P_{DCR} based criterion for the occurrence of the bubble bursting. The blue plane in the plot indicates the bursting threshold corresponding to $P_{DCR} = -28$, as suggested in the work of Mitra and Ramesh (2019). Based on the adopted bursting criterion, most of the acquired flow cases are representative of a short bubble state (i.e. $P_{DCR} > -28$), whereas a part of them is classified as long ones. Interestingly, these latter conditions are characterized by h_r/δ^* and u_{min}/U_e values that are higher than the proposed thresholds for the occurrence of the absolute instability in the laminar separation bubble (see the dashed lines in the plot). Otherwise, all the short bubbles fall within the range typical of convective one, i.e. that of the K-H instability process. What is shown in figure 7 therefore suggests that a link between the change in the bubble state and the modification of its stability characteristics exists, which can be further studied in future works by means of the present experimental database.

CONCLUSIONS

The present work presented a vast experimental data base on laminar separation bubbles forming on a flat plate for variable Reynolds numbers, Tu levels and pressure gradients. The analysis of the time-mean flow distributions combined with the implementation of a bursting criterion previously presented in the literature clearly indicated the occurrence of both short and long bubble states for the different combinations of the flow parameters. This makes the present data set suitable for the characterization of such kind of phenomenon, thus possibly providing engineering correlations for bursting prediction. Moreover, the stability characteristics of the acquired laminar separation bubbles have been shown to be strongly affected by the variation of the external flow conditions. The scale of the vortical structures driving transition, as well as the mechanisms promoting the disturbance growth in the boundary layer have been found to change significantly when varying the flow Reynolds number. Interestingly, the bursting process appears to be strictly linked to the onset of the absolute instability of the separated shear layer. The present experimental data base can be therefore adopted for the study of the separation induced transition for a wide range of flow conditions and the understanding of the under-laying mechanisms driving the switch between a short and a long bubble state. To this end, the present data base is intended to be open and available to the scientific community.

DATA AVAILABILITY STATEMENT

The present data base is open and it is available upon request to the authors.

References

Alferez N, Mary I, Lamballais E (2013) Study of stall development around an airfoil by means of high fidelity large eddy simulation. Flow, turbulence and combustion 91(3):623–641

Almutairi JH, Jones LE, Sandham ND (2010) Intermittent bursting of a laminar separation bubble on an airfoil. AIAA journal 48(2):414–426

Canepa E, Cattanei A, Jafelice F, et al (2018) Effect of rotor deformation and blade loading on the leakage noise in low-speed axial fans. Journal of Sound and Vibration 433:99–123

Canepa E, Cattanei A, Mazzocut Zecchin F (2019) Leakage noise and related flow pattern in a low-speed axial fan with rotating shroud. International Journal of Turbomachinery, Propulsion and Power 4(3):17

Canepa E, Cattanei A, Moradi M, et al (2021) Experimental study of the leakage flow in an axial-flow fan at variable loading. International Journal of Turbomachinery, Propulsion and Power 6(4):40

Charonko JJ, Vlachos PP (2013) Estimation of uncertainty bounds for individual particle image velocimetry measurements from cross-correlation peak ratio. Measurement Science and Technology 24(6):065,301

Crabtree L (1959) The formation of regions of separated flow on wing surfaces. Citeseer

Curle N, Skan S (1957) Approximate methods for predicting separation properties of laminar boundary layers. Aeronautical Quarterly 8(3):257–268

Dellacasagrande M, Barsi D, Lengani D, et al (2020a) Response of a flat plate laminar separation bubble to reynolds number, free-stream turbulence and adverse pressure gradient variation. Experiments in Fluids 61(6)

Dellacasagrande M, Lengani D, Simoni D, et al (2020b) Experimental investigation on the loss production mechanisms in transitional boundary layers. In: Turbo Expo: Power for Land, Sea, and Air, American Society of Mechanical Engineers, p V02ET41A019

Diwan SS, Chetan S, Ramesh O (2006) On the bursting criterion for laminar separation bubbles. In: IUTAM Symposium on Laminar-Turbulent Transition, Springer, pp 401–407

Eljack E, Soria J, Elawad Y, et al (2021) Simulation and characterization of the laminar separation bubble over a naca-0012 airfoil as a function of angle of attack. Physical Review Fluids 6(3):034,701

Gaster M (1967) The structure and behaviour of laminar separation bubbles. Technical report, Aeronautical Research Council

Istvan MS, Kurelek JW, Yarusevych S (2018) Turbulence intensity effects on laminar separation bubbles formed over an airfoil. AIAA Journal 56(4):1335–1347

Marxen O, Henningson DS (2011) The effect of small-amplitude convective disturbances on the size and bursting of a laminar separation bubble. J Fluid Mech 671:1–33

Maucher U, Rist U, Wagner S (2000) Refined interaction method for direct numerical simulation of transition in separation bubbles. AIAA journal 38(8):1385–1393

Mitra A, Ramesh O (2019) New correlation for the prediction of bursting of a laminar separation bubble. AIAA Journal 57(4):1400–1408

Owen P, Klanfer L (1953) On the laminar boundary layer separation from the leading edge of a thin aerofoilv. Tech. rep., Aeronautical Research Council London (United Kingdom)

Pauley LL, Moin P, Reynolds WC (1990) The structure of two-dimensional separation. Journal of Fluid Mechanics 220:397–411

Sciacchitano A, Neal DR, Smith BL, et al (2015) Collaborative framework for piv uncertainty quantification: comparative assessment of methods. Measurement Science and Technology 26(7):074,004

Serna J, Lázaro B (2015) On the bursting condition for transitional separation bubbles. Aerospace Science and Technology 44:43–50

Simoni D, Lengani D, Ubaldi M, et al (2017) Inspection of the dynamic properties of laminar separation bubbles: free-stream turbulence intensity effects for different Reynolds numbers. Exp Fluids 58(6):66

Verdoya J, Dellacasagrande M, Lengani D, et al (2021) Inspection of structures interaction in laminar separation bubbles with extended proper orthogonal decomposition applied to multi-plane particle image velocimetry data. Physics of Fluids 33(4):043,607

Von Doenhoff AE (1938) A preliminary investigation of boundary-layer transition along a flat plate with adverse pressure gradient. Tech. rep.

Wieneke B (2015) PIV uncertainty quantification from correlation statistics. Measurement Science and Technology 26(7):074,002

Wilson BM, Smith BL (2013) Uncertainty on piv mean and fluctuating velocity due to bias and random errors. Measurement Science and Technology 24(3):035,302